Springer
Acta Mechanica Sinica

**• RESEARCH PAPER •**

Acta Mech. Sin., Vol. 40, 523508 (2024)
https://doi.org/10.1007/s10409-024-23508-x

# Energy harvesting and speed sensing with a hybrid rotary generator for self-powered wireless monitoring

Zhixia Wang[1,2,3], Hongyun Qiu[1], Xuanbo Jiao[1], Wei Wang[1,2*], Qichang Zhang[1,2],
Ruilan Tian[3,4], and Dongxing Cao[5]

[1] *School of Mechanical Engineering, Tianjin University, Tianjin 300350, China;*
[2] *Tianjin Key Laboratory of Nonlinear Dynamics and Control, Tianjin 300350, China;*
[3] *State Key Laboratory of Mechanical Behavior and System Safety of Traffic Engineering Structures, Shijiazhuang Tiedao University, Shijiazhuang 050043, China;*
[4] *Department of Mechanics Engineering, Shijiazhuang Tiedao University, Shijiazhuang 050043, China;*
[5] *Faculty of Materials and Manufacturing, Beijing University of Technology, Beijing 100124, China*

Received December 7, 2023; accepted February 21, 2024; published online June 26, 2024

Real-time onboard health monitoring systems are critical for the railway industry to maintain high service quality and operational safety. However, the issue with power supplies for monitoring sensors persists, especially for freight trains that lack onboard power. Here, we propose a hybrid piezoelectric-triboelectric rotary generator (HPT-RG) for energy harvesting and vehicle speed sensing. The HPT-RG incorporates a rotational self-adaptive technique that softens the equivalent stiffness, enabling the piezoelectric non-resonant beam to surpass resonance limitations in a low-frequency region. The experiments demonstrate the feasibility of using the HPT-RG as an energy harvesting module to collect the rotational energy of the freight rail transport and power the wireless temperature sensors. To allow multiple monitoring in confined spaces on trains, a triboelectric sensing module is added to the HPT-RG to sense the operation speed and mileage of vehicles. Furthermore, the generator exhibits favorable mechanical durability under more than 600 h of official testing on the train bogie axle. The proposed HPT-RG is essential for creating a truly self-powered, maintenance-free, and zero-carbon onboard wireless monitoring system on freight railways.

**Energy harvesting, Speed sensing, Rotational self-adaptive technique, Low-frequency, Self-powered wireless monitoring**

**Citation:** Z. Wang, H. Qiu, X. Jiao, W. Wang, Q. Zhang, R. Tian, and D. Cao, Energy harvesting and speed sensing with a hybrid rotary generator for self-powered wireless monitoring, Acta Mech. Sin. 40, 523508 (2024), https://doi.org/10.1007/s10409-024-23508-x

## 1. Introduction

The vibration of wheelsets in railways significantly increases with improved operating speed and carrying capability, subsequently promoting the risk of derailment [1]. It may cause severe damage to the railway track and lead to huge economic losses when trains continue to run with derailed wheelsets undetected [2]. Therefore, vehicles are in urgent need of reliable, long-term, real-time condition monitoring to ensure normal operation and predict potential bogie frame failures. Monitoring systems generally employ various wayside or onboard sensors to evaluate the operational condition and enhance structural reliability for the railway industry [3]. Wayside sensors located in the rails or surrounding areas, detect train faults at specific locations [4], while onboard monitoring systems utilize sensors on trains to provide real-time operational data of vehicles [5]. However, the continuous power supply for these onboard sensors remains challenging since locomotive electric power is not available to freight wagons [6]. In addition, battery-powered sensors incur significant maintenance costs and associated environmental problems due to their limited battery life. Therefore, exploiting an electromechanical

---

*Corresponding author. E-mail address: wwang@tju.edu.cn (Wei Wang)
Executive Editor: Yanqing Wang

conversion structure that collects the mechanical energy of the vehicle or exploring a self-powered sensor without external power sources are of great significance for intelligent freight railways [7]. Generally, the piezoelectric [8,9], triboelectric [10,11], and electromagnetic transduction mechanisms [12,13] harness and convert the mechanical energy of the railways into electricity. Electromagnetic generators exhibit high energy conversion efficiency with mechanical modulation mechanisms under bogie and track excitations, but they have demerits of huge size, poor mobility, and severe impact on the railway environment. While, in addition to providing the advantages of convenient implementation, easy miniaturization, and long-lasting mechanical durability, piezoelectric generators also exhibit excellent output performance [14]. Given that axle temperature and acceleration real-time sensing is crucial for reducing temperature surveillance and wheelset bearing fault diagnosis, onboard sensors integrated with generators are in line with the development trends [15]. Furthermore, freight railways operate at low frequencies, such as 8.4-11.6 Hz in rotational motion [16] and 2.9-8 Hz [17] in lateral reciprocating motion under typical freight speeds in China, and the generators should possess brilliant robustness at a wider low-frequency range.

Generators that convert the reciprocating motion of the bogies in vehicles into electricity have been extensively studied for decades [18]. For instance, Fu et al. [19] designed a broadband generator for vertical vibration of the bogie by coupling nonlinear magnetic force and multi-mode vibration. Wang et al. [20] developed an ultralow-frequency and broadband generator with a hybrid nonlinear mechanism. Deployed on the axle box, the device scavenged the lateral vibrations of the bogie. Nevertheless, these generators require complex nonlinear mechanisms to match the low-frequency and broadband vibrations of freight trains, which takes up additional space and reduces the power density. The rotation-to-vibration mechanism has become the recent trend to convert mechanical rotation into electricity because of its frequency self-tuning function with centrifugal force [21]. Furthermore, the self-powered sensors mounted on rotary axle monitor shaft temperature and acceleration more accurately than those deployed on stationary parts. Guan and Liao [22] introduced a self-tuning energy generator with a wide operation bandwidth from 7 to 13.5 Hz. Gu and Livermore [23] further adopted centrifugal force to the radial beam and achieved a distributed operation bandwidth of 6.2-16.2 Hz. Rui et al. [24] investigated the effect of the centrifugal force on the resonant frequency for a radially inverted beam. Simulations and experiments demonstrated a 29.3%-63.1% reduction in the resonant frequency when the center distance of the inertial mass was 0-5 times the cantilever length. Lu et al. [25] investigated a nonlinear magnet-coupled double-beam generator that provided a wide range rotational frequency from 1.7 to 6.2 Hz. Unfortunately, the equivalent stiffness of the piezoelectric beam skipped to a negative value, causing the generator to enter a nonoscillatory deflected mode, leading to a dramatic drop in the output power [26]. Moreover, the generated power is proportional to the cube of the resonant frequency, and thus the output of these generators may be insufficient to power sensors under low-frequency excitations [27].

To achieve high output power under low-frequency excitations, researchers have proposed frequency up-conversion techniques, including magnetic plucking and impact mechanisms [28]. Pillatsch et al. [29] combined an eccentric rotating disk and magnetic repulsion to make the piezoelectric beam vibrate, realizing a 400 Hz oscillation at a 2 Hz excitation. Fu and Yeatman [30] provided a bistability rotary generator, where the magnetic repulsion force acted as the excitation force of the piezoelectric beam to produce electricity. Furthermore, Zou et al. [31] compounded the magnetic repulsion force and the flex tensional mechanism to convert low-frequency rotation into high-frequency vibration. Hu et al. [32] amplified the excitation frequency by utilizing nonlinear magnetic force and accelerating gear. The split design of the rotational and vibrational components, installed in different positions, renders the miniaturization of these nonlinear magnetic devices difficult and unsuitable for the limited installation space [33]. It is imperative to investigate high-performance generators with compact sizes, as the bearing temperature monitoring system in freight trains imposes strict requirements on the volume of the generator [34]. Gu and Livermore [35] employed a subsystem that accommodated low-frequency motion and triggered another high-frequency subsystem for electricity generation. They achieved a power density of 30.8 μW $\mathrm{cm}^{-3}$ with an operating bandwidth of 11 Hz. Rui et al. [36] designed a rotary generator with a peak power of 52.1 μW at 4.2 Hz, where the low-frequency beam was confined by piezoelectric and protection beams within 2.6-4.5 Hz. Fang et al. [37] presented a rotational impact generator for low-frequency excitations and demonstrated that the centrifugal force was capable of amplifying the relative displacement to improve energy harvesting performance [38]. Zhao et al. [39] introduced a maximal utilization strategy for energy harvesting in a broad speed range (0-1000 r $\mathrm{min}^{-1}$). Ramírez et al. [40] demonstrated an E-shape multi-beam rotary generator with a maximum power of 200 μW that operated at a low frequency of 0.5 to 3 Hz. Yang et al. [41] used an elastic ball to hit the piezoelectric beam, resulting in an output power of 613 μW at 3.3 Hz. Tan et al. [42] developed a battery-like self-charge universal module for low-frequency applications with an impact mechanism. However, due to the relatively simple structure, the impact causes energy loss, thereby reducing the number of self-powered sensors in the confined space.

At the same time, developing self-powered sensors that do not require an external power source is essential for addressing the energy supply of surveillance systems. Triboelectric nanogenerators, due to their extreme sensitivity to vibration, have garnered significant attention from the industry and academia for their potential as self-powered sensors [43]. Wu et al. [44] designed a green energy tire based on triboelectric nanogenerators that not only generated electrical signals but also measured tire pressure and road conditions. Zhao et al. [45] developed a self-powered triboelectric vibration accelerometer, which was able to measure accelerations ranging from 1.07 to 1.25 m $s^{-2}$. Yang et al. [46] reported a triboelectric micromotor by coupling a micromotor and a triboelectric nanogenerator. Zheng et al. [47] proposed a self-powered smart transportation infrastructure skin, incorporating triboelectric nanogenerators and artificial intelligence. Self-powered wireless sensor nodes with triboelectric nanogenerators have achieved remarkable results in numerous areas. Therefore, we propose the integration of an energy harvesting and sensing device by combining a triboelectric sensing module with the harvesting module to achieve comprehensive monitoring of the axle box within a limited space for freight trains.

In this work, we propose a hybrid piezoelectric-triboelectric rotary generator (HPT-RG) with resonant and non-resonant beams, and a triboelectric sensing module for energy harvesting and speed sensing in vehicles. The resonant beam converts the low-frequency excitation into the high-frequency vibration of the non-resonant beam with an impact mechanism. Instead of needing to be in a resonance state, the non-resonant beam produces high-frequency vibrations in virtue of the resonant beam. The piezoelectric module and triboelectric module convert electricity to enable self-powered axle temperature and operation speed/mileage sensing of the train, as shown in Fig. 1(a). The contributions of this study are as follows: (1) the non-resonant beam effectively converts the low-frequency energy and protects the resonant beam from entering the deflected mode; (2) by optimizing structural parameters, the HPT-RG was designed to oscillate effectively in the frequency range of 8.4-10.4 Hz, which corresponds to the vibration characteristics of freight trains; (3) the theoretical and experimental results indicate that the rotational self-adaptive technology effectively overcomes the resonance restriction of the piezoelectric beam, achieving a maximum power output of 1.23 mW with a power density of 0.722 mW $cm^{-3}$; (4) in terms of applications, the harvesting module powers a wireless temperature sensor, while the triboelectric module acts as a self-powered sensor and detects the motion state of the train wheel hub.

## 2. Design and working principle

Due to the narrow diameter of the axles in the wheelsets, such as 150 mm in the common K6 bogies, the available space for deploying the generators is severely restricted. To reach multi-sensing within a limited space, the HPT-RG not only converts rotational energy into electricity to power sensors but also serves as a speedometer for freight trains. The schematic diagram of the assembled prototype is shown in Fig. 1(b). The HPT-RG mainly comprises a resonant beam, up and down non-resonant beams, and a triboelectric sensing module. Instead of needing to be in a resonance state, the non-resonant beam produces high-frequency vibrations under low-frequency and broadband excitations in virtue of the resonant beam. The electromechanical coupling model of the HPT-RG is simplified as depicted in Fig. 1(c), where $m$, $c$, $k$, $u$, $e$, and $R_{\mathrm{L}}$ denote the equivalent mass, damping, stiffness, tip displacement of the beam, the gap distance between the resonant beam and non-resonant beam, and external resistance, respectively; the subscripts r and n denote the resonant and non-resonant beam.

The working principle of the HPT-RG is as follows: (1) when HPT-RG is mounted on a rotational shaft, the resonant beam generates vibration and couples the high-frequency non-resonant beams to vibrate for a short time due to the inertial mass gravity acting as a periodic excitation to transform rotary motion into the vibration of the resonant beam; (2) the non-resonant beam responds with high frequency to low-frequency excitation by vibrating with exponentially attenuating amplitude at its resonant frequency; (3) in addition to causing periodic tension and compression of the macro fiber composite (MFC) to bring about electric output according to the $d_{31}$ piezoelectric effect, the vibration of HPT-RG also facilitates the triboelectric sensing module to generate pulse voltage and directly provide feedback on the operation speed and mileage of vehicles.

Figure 1(d) depicts the power generation of HPT-RG in four states. The symmetric structure allows the down non-resonant beam and the corresponding triboelectric sensing module to be selected as representatives. At stage S1, the device begins to rotate, and no current is generated in the MFC due to non-deflection. After that, the resonant beam makes contact with the down non-resonant beam and moves synchronously to its maximum displacement in stage S2. The non-resonant beam couples with the resonant beam for a period, then disengages from the resonant beam and experiences attenuated vibration until the next coupled vibration in stage S2. This is, the non-resonant beam undergoes attenuation vibration from S2 to S4. Consequently, the non-resonant beams continually repeat the above processes to generate a continuous alternating current (AC) based on the piezoelectric effect. In addition, Fig. 1(d) also illustrates the voltage generation of the triboelectric

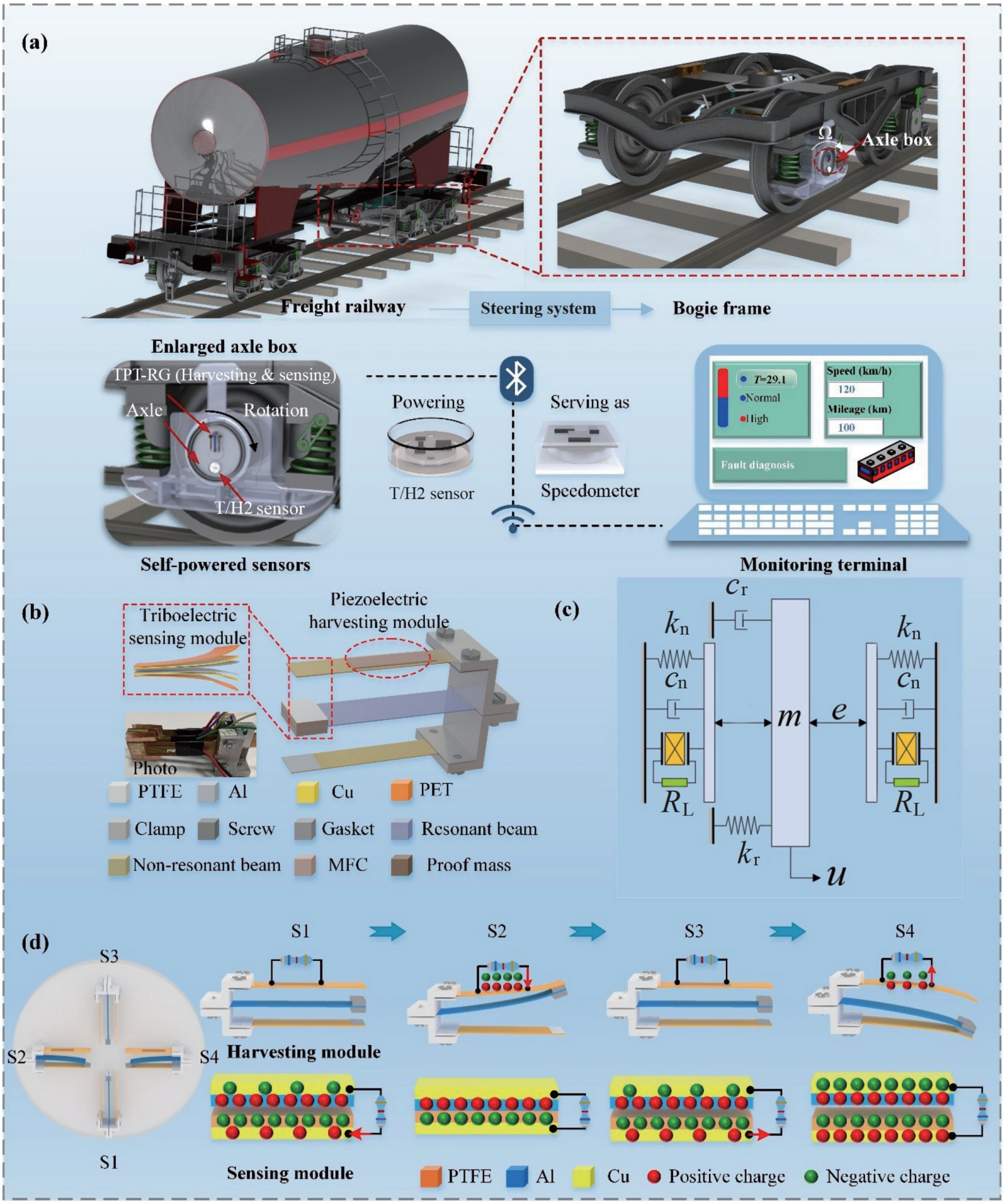

**Figure 1** (a) Illustration of the HPT-RG to realize a self-powered axle temperature and speed/mileage monitoring system for the railway industry; (b) structure design and a digital photo of the HPT-RG; (c) equivalent electromechanical coupling system of the HPT-RG; (d) working principle of piezoelectric harvesting module and triboelectric sensing module in HPT-RG.

sensing module. At stage S2, the poly tetra fluoroethylene (PTFE) and Al surfaces generate negative and positive charges, respectively, due to contact electrification. As tribolayers extend away from each other in stage S3, the positive charges transfer from the PTFE electrode to the Al electrode, establishing an equilibrium electric field. At stage S4, the charge remains stable, and no current flows in the external circuit. Subsequently, as the PTFE moves gradually towards the Al electrode, an opposite current is induced in stage S1. A pulsed signal is generated in the triboelectric module due to contact electrification and electrostatic induction.

## 3. Modeling and dynamic analysis of the HPT-RG

### 3.1 Theoretical modeling of the resonant beam

To comprehend the operating principle, it is essential to formulate a theoretical model of the resonant beam. Assuming that the amplitude of the resonant beam is small, the system can be approximated as an inertial mass oscillating along a linear path [48], as depicted in Fig. 2(a).

The displacement of the mass $m$ relative to the origin of the coordinate is $u(t)$, and the angle with the $y$-axis is $\theta(t)$, then the displacement in the Cartesian coordinate is

$$r = u\sin\theta i - u\cos\theta j. \tag{1}$$

Differentiating Eq. (1) concerning $t$ obtains the speed

$$\dot{r} = (\dot{u}\sin\theta + u\dot{\theta}\cos\theta)i - (\dot{u}\cos\theta - u\dot{\theta}\sin\theta)j. \tag{2}$$

Based on Eq. (2), the kinetic energy and potential energy of the system are, respectively, expressed as

$$T = \frac{1}{2}m\dot{r}^2 = \frac{1}{2}m\left(\dot{u}^2 + u^2\dot{\theta}^2\right), \tag{3}$$

$$U = \frac{1}{2}k_{\mathrm{r}}u^2 - umg\cos\theta. \tag{4}$$

Combining Eqs. (3) and (4), we have the Euler-Lagrange equation

$$L = T - U = \frac{1}{2}m\left(\dot{u}^2 + u^2\dot{\theta}^2\right) - \frac{1}{2}k_{\mathrm{r}}u^2 + umg\cos\theta. \tag{5}$$

For the displacement $u$, the system response is

$$\frac{\mathrm{d}}{\mathrm{d}t}\left(\frac{\partial L}{\partial \dot{u}}\right) - \frac{\partial L}{\partial u} = -c_{\mathrm{r}}\dot{u}. \tag{6}$$

On account of Eq. (5), Eq. (6) becomes

$$m\ddot{u} - m\dot{\theta}^2 u + k_{\mathrm{r}}u + c_{\mathrm{r}}\dot{u} - mg\cos\theta = 0, \tag{7}$$

where the rotation angle $\theta = \Omega t$, with $\Omega$ being the rotational frequency of the freight wheel axle. So that Eq. (7) simplifies as

$$m\ddot{u} + c_{\mathrm{r}}\dot{u} + \left(k_{\mathrm{r}} - m\Omega^2\right)u = mg\cos(\Omega t). \tag{8}$$

According to Eq. (8), the equivalent stiffness of the resonant beam varies with rotational frequency, that is, the resonant beam possesses a rotational self-adaptive feature for gravity as periodic excitation.

In some instances, the center of the inertial mass in the resonant beam deviates from the rotational center, resulting in a centripetal force acting on the resonant beam. The developing dynamic models with different centrifugal force forms (a) compressed and (b) stretched effects for the resonant beam (see Appendix for details). To improve the sensitivity of the axle temperature monitoring, this work adopted the HPT-RG integrated with the temperature sensor on the axle end, with the center of the inertial mass coinciding with the rotational center.

### 3.2 The dynamic modeling of the HPT-RG

The lumped parameter model of the HPT-RG under the base excitation is shown in Fig. 1(c), and the detailed parameters are given in Table 1. The dynamic behavior of the HPT-RG can be classified into two cases depending on the relationship between the displacement of the resonant beam $u$ and the gap distance $e$. In the first case, the resonant beam vibrates with the damping $c_{\mathrm{r}}$ and stiffness $k_{\mathrm{r}}$ under periodic excitation from gravity, when $u$ is less than or equal to $e$. The resonant frequency of the non-resonant beam is sufficiently far away from the excitation frequency so that its position remains fundamentally fixed. In the second case, the resonant beam couples with the non-resonant beam and vibrates together for a certain period with additional damping $c_{\mathrm{n}}$ and stiffness $k_{\mathrm{n}}$ under $u$ above the gap distance $e$. Therefore, according to Newton's second law, the piecewise governing equations of the resonant beam are given by

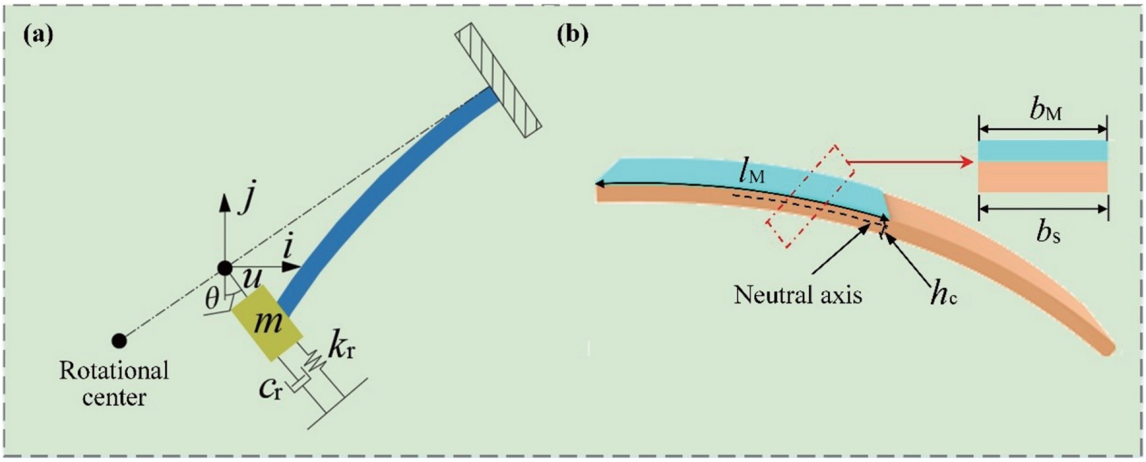

**Figure 2** (a) Mechanical model of the resonant beam; (b) 3D view and cross-sectional view of the non-resonant beam.

**Table 1** Geometric and physical parameters of the proposed HPT-RG

| Parameter | Value |
|---|---|
| Resonant beam dimensions $l_r \times b_r \times h_r$ (mm) | 60 × 10 × 0.3 |
| Non-resonant beam dimensions $l \times b_n \times h_n$ (mm) | 50 × 10 × 0.5 |
| MFC patch dimensions $l_M \times b_M \times h_M$ (mm) | 37 × 10 × 0.3 |
| Equivalent mass of resonant beam $m$ (g) | 13.2 |
| Young's modulus of substrate $E_s$ (GPa) | 128 |
| Young's modulus of MFC $E_M$ (GPa) | 30.336 |
| Capacitance $C_p$ (nF) | 20 |
| piezoelectric coefficient $d_{31}$ (pC N$^{-1}$) | $-1.7 \times 10^2$ |
| Equivalent damping coefficient of resonant beam $c_r$ (Ns m$^{-1}$) | 0.0109 |
| Equivalent damping coefficient of non-resonant beam $c_n$ (Ns m$^{-1}$) | 0.0267 |

$$\begin{cases} m\ddot{u} + c_r\dot{u} + \left(k_r - m\Omega^2\right)u = mg\cos(\Omega t), & |u| < e, \\ m\ddot{u} + (c_r + c_n)\dot{u} + \left(k_r + k_n - m\Omega^2\right)u \mp k_n e & \\ = mg\cos(\Omega t), & |u| > e. \end{cases} \tag{9}$$

With the log decrement method, the natural frequency and damping ratio of the resonant beam is $\omega_r$ = 58.5 rad s$^{-1}$ and $\xi_r$ = 0.015 rad s$^{-1}$, respectively. Similarly, the parameters of the non-resonant beam have been determined as $\omega_n$ = 140.6 rad s$^{-1}$ and $\xi_n$ = 0.033 rad s$^{-1}$. Based on $c = 2m\xi\omega$, we determine the damping coefficients $c_r$ and $c_n$ as 0.0109 and 0.0267 Ns m$^{-1}$, respectively. Figure 2(b) describes the 3D and cross-sectional view of an unimorph non-resonant beam. Due to the MFC on the substrate, the distance between the neutral surface of the non-resonant beam and the substrate surface is

$$h_c = \frac{E_s b_s h_s^2 - E_M b_M h_M^2}{2\left(E_M b_M h_M + E_s b_s h_s\right)}, \tag{10}$$

where $E$, $b$, and $h$ denote Young's modulus, width, and height, respectively; the subscripts s and M denote the substrate and MFC of the non-resonant beam. The equivalent stiffness of the non-resonant beam is

$$k_n = \left\{\left[\frac{l_M^3 + 3l_M^2\left(l - l_M\right) + 3l_M\left(l - l_M\right)^2}{3D_c}\right] + \frac{\left(l - l_M\right)^3}{3D_s}\right\}^{-1}, \tag{11}$$

where $D_c$ and $D_s$ are the bending stiffness of the composite beam and substrate,

$$\begin{cases} D_s = \dfrac{E_s b_s h_s^3}{12}, \\ D_c = \dfrac{E_M b_M h_M^3}{12} + E_M\left(b_M t_M\right)\left(\dfrac{h_M}{2} + h_c\right)^2 \\ \qquad + \dfrac{E_s b_s h_s^3}{12} + E_s b_s h_s\left(\dfrac{h_s}{2} - h_c\right)^2. \end{cases} \tag{12}$$

Based on the derived models, we carried out a parameter study for the gap distance $e$ to optimize the power generation before experiment verification within 7-15 Hz due to the typical freight operating 80-120 km h$^{-1}$, with the corresponding rotation frequency of 8.4-11.6 Hz, as illustrated in Fig. 3(a). The increase in gap distance $e$ serves to gradually shift the operation frequency to low-frequencies, concurrently, increasing the amplitude of the resonant beam. To visualize the relationship between the gap distance and the dynamic characteristics of the HPT-RG, the maximum amplitudes and corresponding frequencies at 2-10 mm were marked by a purpled line in the contour map. Referring to Fig. 3(b) obtains that $e \in [2, 4]$ mm: the amplitude arrived at the peak value at 15 Hz; $e \in [4, 10]$ mm: the frequency corresponding to the peak-amplitude ratio gradually decreased with the growth of the gap distance. From the amplitude-frequency response in Fig. 3(b), we also conclude that the resonant beam and non-resonant beam exhibited coupled vibration with relatively large amplitude under broadband frequency at a 5 mm gap distance.

Figure 3(c) shows the amplitude-frequency response and displacement-velocity phase of the HPT-RG under 8.4, 11.6, and 15 Hz (corresponding to the typical freight train speeds of 80, 120 km h$^{-1}$, and a low-level amplitude motion) with $e$ = 5 mm, respectively. The prototype possesses three equilibrium positions due to the piecewise linearity induced by the impact between the resonant and non-resonant beams. The device passed through the bistable state (8.4 Hz) to the interwell motion state (11.6 Hz) and finally into a small amplitude monostable state (15 Hz) with increasing frequency. Furthermore, the maximum displacement of the resonant beam exceeded the gap distance $e$ in the range of 7-14.6 Hz, indicating that the piezoelectric harvesting and triboelectric sensing modules worked efficiently at train speeds. The equivalent stiffness of the resonant beam became negative when the gravity force exceeded its restoring force at 15 Hz, causing the HPT-RG to exhibit monostable motion and fall into deflection mode.

### 3.3 Output characteristics of the HPT-RG

To obtain the output voltage, we derive the stress of the MFC at position ($\upsilon$, $u$)

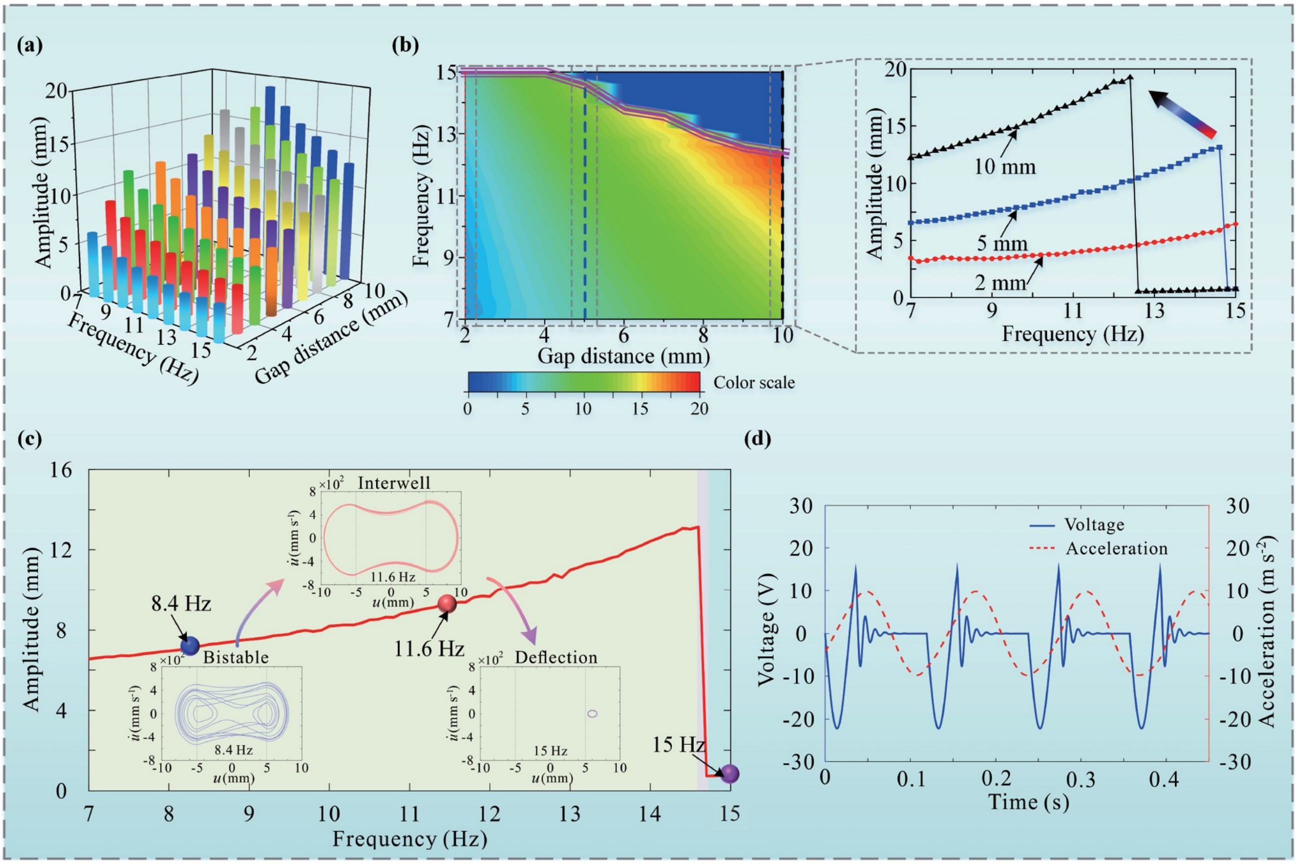

**Figure 3** Comparison of amplitude of the resonant beam with various gap distances for (a) 3D view and (b) contour 2D view of the amplitude-frequency response of the generator. (c) Amplitude-frequency response of the HPT-RG under $e$ = 5 mm and the corresponding phase diagrams at typical frequencies, such as typical freight train speeds of 80, 120 km h$^{-1}$, and a low-level amplitude motion, corresponding frequencies of 8.4, 11.6, and 15 Hz. (d) Voltage response of the HPT-RG under 8.4 Hz at $e$ = 5 mm.

$$\sigma(v,u)=\frac{k_{\mathrm{n}}U_0E_{\mathrm{M}}}{D_{\mathrm{c}}}(1-v)(u-h_{\mathrm{c}}), \tag{13}$$

where $U_0$ is the displacement of the resonant beam. Hence, the induced electric field is

$$\begin{aligned}E(v,u)&=\left(\frac{d_{31}}{\varepsilon_{\mathrm{r}}\varepsilon_0}\right)\times\sigma(v,u)\\&=\frac{d_{31}k_{\mathrm{n}}U_0E_{\mathrm{M}}}{\varepsilon_{\mathrm{r}}\varepsilon_0D_{\mathrm{c}}}(l-v)(u-h_{\mathrm{c}}),\end{aligned} \tag{14}$$

where $d_{31}$, $\varepsilon_0$, and $\varepsilon_{\mathrm{r}}$ are the piezoelectric coefficient, the permittivity of vacuum, and the permittivity of the MFC, respectively. Based on Eq. (14), we acquire the output voltage of the MFC

$$\begin{aligned}V_{\mathrm{ave}}&=\frac{1}{l_{\mathrm{M}}}\int_0^{l_{\mathrm{M}}}\int_0^{h_{\mathrm{M}}}E(v,u)\mathrm{d}u\mathrm{d}v\\&=\left(\frac{2l-l_{\mathrm{M}}}{2}\right)\frac{d_{31}k_{\mathrm{n}}U_0E_{\mathrm{M}}}{\varepsilon_{\mathrm{r}}\varepsilon_0D_{\mathrm{c}}}\left(\frac{1}{2}h_{\mathrm{M}}^2-h_{\mathrm{c}}h_{\mathrm{M}}\right).\end{aligned} \tag{15}$$

Substituting the displacement $u(t)$ into Eq. (15) obtains the output voltage

$$V_{\mathrm{oc}}(u)=\left(\frac{2l-l_{\mathrm{M}}}{2}\right)\frac{d_{31}k_{\mathrm{n}}E_{\mathrm{M}}}{\varepsilon_{\mathrm{r}}\varepsilon_0D_{\mathrm{c}}}\left(\frac{1}{2}h_{\mathrm{M}}^2-h_{\mathrm{c}}h_{\mathrm{M}}\right)(u-e). \tag{16}$$

The output characterization of the HPT-RG is investigated by taking the up non-resonant beam as an example due to its symmetric structure. Figure 3(d) illustrates the voltage response of the up non-resonant beam at $e$ = 5 mm under 8.4 Hz based on Eq. (16). The resonant beam impacted the non-resonant beam, resulting in a coupled vibration with a frequency of 27.8 Hz. After a short period of coupled vibration, the non-resonant beam separated from the synchronized motion and entered into a decaying oscillation at its resonance frequency of 86.8 Hz until it impacted the resonant beam again. Therefore, the HPT-RG successfully generated an output voltage of 86.8 Hz at 8.4 Hz excitation.

## 4. Performance investigation

### 4.1 Prototype fabrication and experimental setup

A close-up view of the proposed HPT-RG is shown in Fig. 4(a). Piezoelectric layer MFC (model: M2807 P2, Smart Material Corp.) was laminated near the fixed end of the beryllium bronze substrate for energy conversion, while

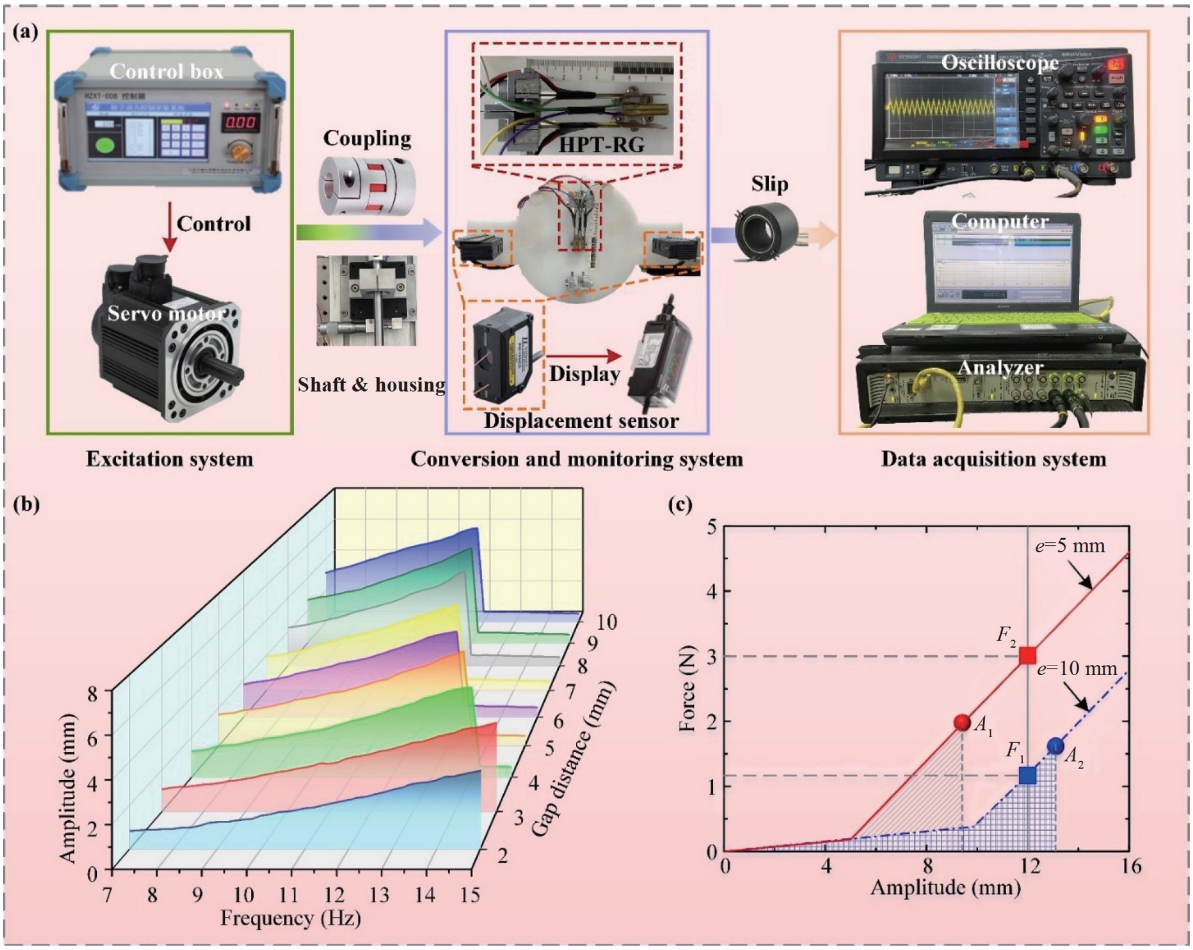

**Figure 4** (a) Experimental setup and process to test HPT-RG in the lab; (b) amplitude-frequency responses of the non-resonant beam under different gap distances; (c) force-displacement relations of the resonant beam.

copper counterweight was attached to its free end to serve as a proof mass, thereby forming the non-resonant beam. The resonant and non-resonant beams achieved the purpose of free-end alignment using an aluminum double-corner structure. The surface of the proof mass covered a 20 mm × 20 mm × 50 μm PTFE layer as triboelectric material, and the inner surface of the non-resonant beam pasted the same size Al layer as another triboelectric material. The plasma cleaner (model: YZD08-2C, Saot Technology Co., Ltd.) treated the outside surface of PTFE and Al tribolayers to their roughness. A 50 μm Cu electrode covered the inside surface of tribolayers. It is worth noting that a 50 μm polyethylene terephthalate (PET) layer was attached to the Cu film to prevent the charge transfers from the double-corner structure. The gaskets adjusted the initial distance *e*. The whole volume and weight of the prototype are 3.4 $\mathrm{cm}^3$ and 68.36 g, respectively. When considering the volume and weight of fright vehicles, the impact of the prototype on the vehicles is negligible.

To maintain smooth operation and prevent external vibrations from affecting the rotation, the rotor test rig was mounted on an optical vibration isolation platform, as shown in Fig. 4(a). A servo motor integrated with a speed control box (model: HZXT-008, Wuxi Houde Automation Meter Co., Ltd.) drove the rotation system. The proposed prototype was deployed symmetrically at the rotation center within the error limit. An oscilloscope (model: DSOX1204G, Keysight) and an analyzer (model: 3039, B&K) recorded the voltage output and tip displacement of the non-resonant beam through a slip ring (model: 1500 $\mathrm{r\ min}^{-1}$ high-speed slip ring, Senring), respectively. We arranged the laser displacement sensor and the prototyped HPT-RG in a centrosymmetric manner, such that the center of mass coincided with the center of rotation. Since the tip mass of the resonant beam was located at the rotary center and the mass of the resonant beam was considerably smaller than the inertial mass, we only symmetrically arranged the double-corner structure. A micrometer (model: 0-10 micrometer, LINKS) measured the center of the rotary shaft. The micro displacement platform and gasket calibrated the horizontal and vertical center of the shaft, respectively.

## 4.2 Characterization

To validate the theoretical results, the amplitude-frequency responses of the prototyped HPT-RG were measured and calculated for different gap distances within the range of 7-15 Hz with a 0.2 Hz interval, as shown in Fig. 4(a). The non-resonant beams surrounded the resonant beam in the prototyped HPT-RG, and the amplitude of the non-resonant beam coupled with the gap distance represents the amplitude of the resonant beam. Therefore, we directly measured the dynamic characteristics of the non-resonant beam. Figure 4(b) shows the amplitude-frequency responses of the non-resonant beam at 7-15 Hz when the gap distance varied from 2 to 10 mm. The amplitude of the non-resonant beam synchronously increased with the increase of gap distance, while the corresponding operation frequency gradually shifted to low-frequencies.

To explain this phenomenon, the force-displacement relationship of the resonant beam was considered, as illustrated in Fig. 4(c). Under identical excitations, the prototype accumulated the same amount of energy, which resulted in the area covered by amplitude $A_1$ being equal to that of $A_2$. As the ratio of coupling stiffness decreases with increasing gap distance, the system compensates for the whole energy by increasing the amplitude. Therefore, the gap distance is positively correlated with the amplitude of the non-resonant beam. Moreover, for the same displacement, the structure with a larger gap distance has a smaller equivalent restoring force ($F_2 < F_1$), which leads to a lower vibration frequency, resulting in the operation frequency deflecting to low frequencies with a larger gap distance.

The peak displacements and corresponding frequencies of the resonant beam under different gap distances were obtained via simulations and experiments, as presented in Fig. 5(a). As the non-resonant beams encompassed the resonant beam in the prototype, we measured the characteristics of the non-resonant beam using a displacement laser sensor. In this way, the experimental results for the resonant beam at coupled vibrations were obtained by superimposing the measured amplitudes of the non-resonant beam and the gap distance. The non-resonant beam already oscillated at 7 Hz, which was considered the starting point. Namely, when the maximum amplitude appears at higher frequencies, the device possesses a wide bandwidth. The experimental results were in perfect qualitative agreement with the numerical simulations. The slight discrepancy in frequency bandwidth and amplitude is most likely due to the assumption of completely inelastic in the simulations.

In Fig. 6(a), we investigated the output performance of the HPT-RG and calculated the maximum power across load resistances ranging from 100 to 1000 kΩ at frequencies from 7 to 15 Hz. The optimal resistance remained at about 200 kΩ within the frequency range of 7-15 Hz under $e$ = 5 mm. The inset of Fig. 6(a) displays the output voltage and power versus load resistance at typical frequencies of freight trains. The output voltage increased and gradually saturated as the load resistance increased. The HPT-RG delivered maximum power at a matched resistance of around 200 kΩ. Furthermore, the maximum power increased with increasing vehicle speed.

The HPT-RG yielded satisfactory average powers at typical frequencies of freight trains. Figure 6(b) shows the root mean square (RMS) output voltage and corresponding average power of up non-resonant beam at 7-15 Hz with the optimal resistance. It manifested that the output power with optimal resistance increased gradually until it reached the maximum value of 1.23 mW at 13 Hz, and then decreased rapidly. The variation trend of output power versus excitation frequency is consistent with its amplitude-frequency responses.

### 4.3 Performance comparison

Figure 7(a) and Table 2 compare the HPT-RG prototype with recently reported low-frequency rotary generators in

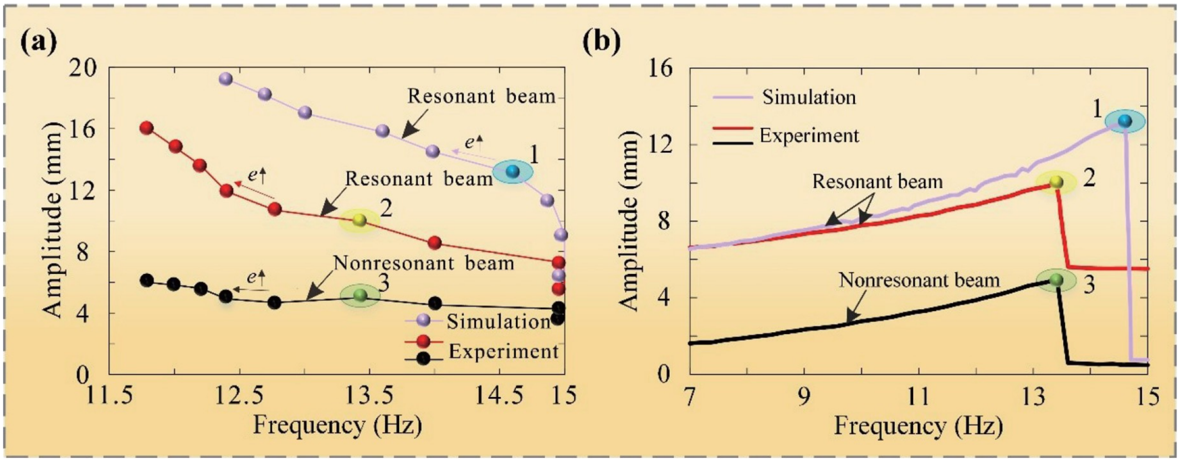

**Figure 5** (a) Operational frequency bandwidth under different gap distances with simulated and experimental methods; (b) corresponding amplitude of the resonant beam at $e$ = 5 mm.

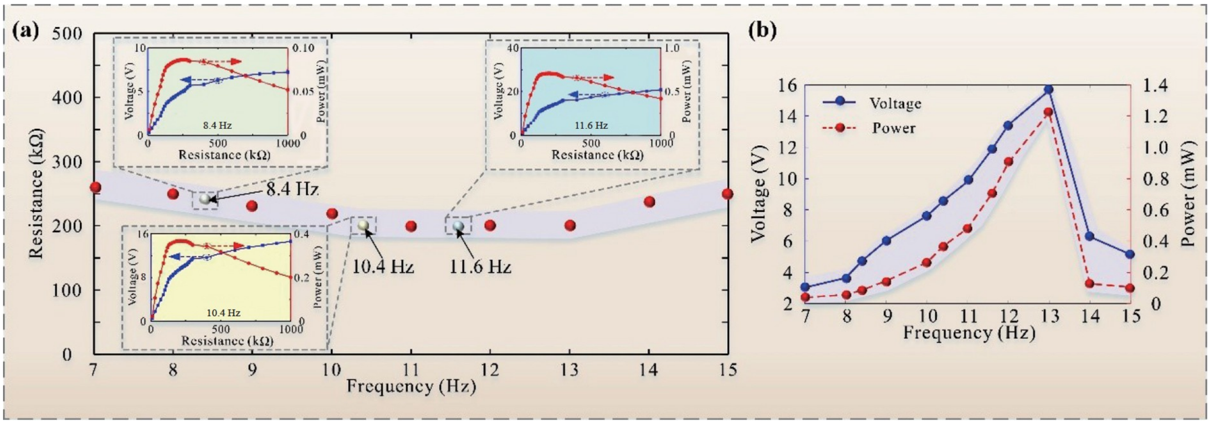

**Figure 6** (a) Optimal resistance of the HPT-RG under 7-15 Hz at *e* = 5 mm; (b) RMS voltage and corresponding power of the up non-resonant beam in HPT-RG with optimal resistance under 7-15 Hz at *e* = 5 mm.

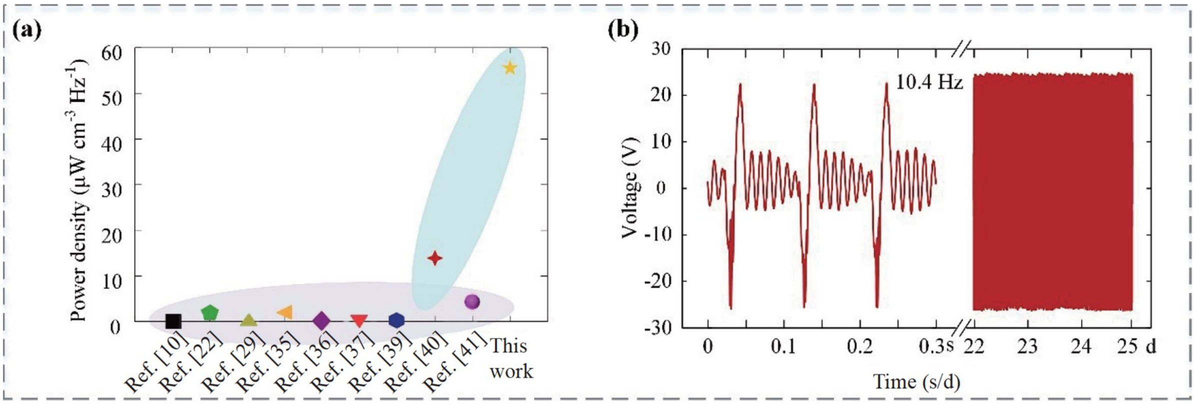

**Figure 7** (a) Power density comparison of the HPT-RG with recently reported low-frequency rotary harvesters; (b) output stability and mechanical durability of the HPT-RG.

**Table 2** Performance comparison between the proposed HPT-RG and recently reported low-frequency rotary piezoelectric harvesters[a)]

| Ref. | Voltage bandwidth (Hz) | Operation conditions (excitation level and resistance) | Power density (μW cm$^{-3}$ Hz$^{-1}$) |
|---|---|---|---|
| [10] | 5-30 | 20 Hz, 3 MΩ | 0.019 |
| [22] | 7-13.5 | 13.5 Hz, unknown | 2.02 |
| [29] | 0.83-16.67 | 16.67 Hz, 81 MΩ/1 MΩ/7 Ω | 0.267 |
| [35] | 4-15.2 | 15.2 Hz, 220 kΩ | 2.02 |
| [36] | 2.6-4.5 | 4.2 Hz, 610 kΩ | 0.133 |
| [37] | 8-12.5 | 11.5 Hz, 6.8 kΩ | 0.00653 |
| [39] | 0.5-3 | 3 Hz, 1000 kΩ | 0.476 |
| [40] | N/A | 3.33 Hz, 20 kΩ | 13.9 |
| [41] | 0.5-4 | 2 Hz, 150 kΩ | 4.3 |
| This work | 7-13 | 13 Hz, 200 kΩ | 55.52 |

a) N/A indicates that the relevant data is not available in the reference.

terms of operating conditions, voltage bandwidth, and power density. Operation conditions and its volume are closely related to the performance of the harvester. Because the excitation amplitude of the rotary beam is the same according to Eq. (8), the normalized power density is defined as the output power divided by the harvester volume and rotational speed, which is relatively valid to evaluate the energy harvesting property. The HPT-RG demonstrates superior output power density at low frequencies of 7-13 Hz, which covers the representative frequencies of freight trains, compared to other devices. While the devices in Refs. [20,32] can also scavenge mechanical energy from freight trains, the power density of the HPT-RG exceeds that of these two prototypes by more than 27 times. Owing to the small volume, harvesters can be symmetrically installed on the axle box and embedded in the axle of the wheelset to improve output power without impacting the performance of bogie frames. This means that the proposed prototype successfully delivers abundant electrical power to the wireless intelligent monitoring network. Furthermore, the output stability and mechanical durability of the HPT-RG were tested by comparing its output voltage after 25 d of its initial use, as shown in Fig. 7(b).

## 4.4 Practical applications

We conducted experiments to evaluate the HPT-RG prototype's potential as a power source for wireless sensors, specifically for transmitting temperature and humidity data. The AC voltage was rectified by a full-bridge rectifier module (model: DB101S), and the rectified electricity was stored in a 100 μF capacitor (model: 1210). A Zener diode (model: SOD-123) was connected in parallel with the capacitor to ensure a stable voltage. Figure 8(a) illustrates that the temperature and humidity sensor (model: T/H2, Xiaomi Co., Ltd.) turned on wirelessly after charging for 3 s and transmitted signals to the receiver every 0.5 s at 11.6 Hz. The excitation source motor stopped for a while and then resumed at 11.6 Hz. The T/H2 sensor continued to operate until the voltage dropped to its threshold of 2 V at 22 s with

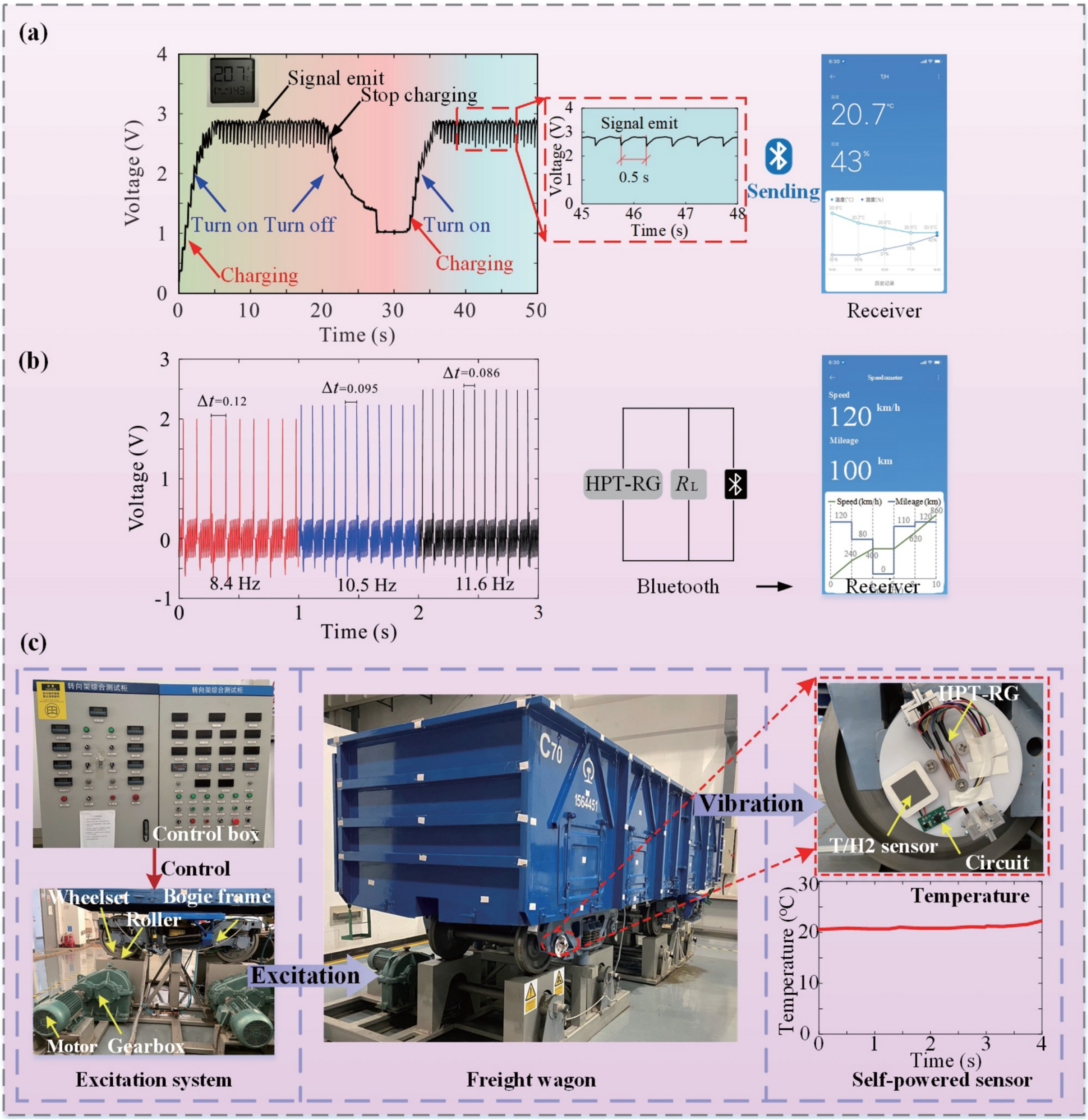

**Figure 8** (a) Demonstration of powering commercial wireless Bluetooth sensor under 11.6 Hz; (b) HPT-RG as a self-powered speed sensor to monitor the operational condition of vehicles; (c) self-powered wireless shaft temperature monitoring with the HPT-RG during the railway simulation tests.

the HPT-RG stopped. The voltage gradually increased and reached the threshold, prompting the T/H2 to operate again when the speed was reset to 11.6 Hz. While it is true that a generator with two non-resonant beams provides high power, the output power of the up non-resonant beam alone was sufficient to power the T/H2 sensor, so we only used one non-resonant beam to power the sensor in our experiments. These results suggest that the HPT-RG can drive additional low-power sensors simultaneously at train speeds.

A voltage difference between the electrodes in the triboelectric sensing module drove a current for the contact and separation of the resonant and non-resonant beams. In this way, the HPT-RG generated a pulse signal at each turn, and it was possible to obtain not the rotary speed but the operation mileage. According to the intervals between the two adjacent peaks in the pulse signals $\Delta t$, one obtains the rotary speed

$$V_{\mathrm{r}}=60/\Delta t. \tag{17}$$

Then, the operation mileage $L_{\mathrm{r}}$ of the vehicle is

$$L_{\mathrm{r}}=\int_0^t \pi D_{\mathrm{w}} V_{\mathrm{r}} \mathrm{d}t, \tag{18}$$

with $D_{\mathrm{w}}$ being the diameter of the wheelset. To investigate the accuracy of the results, we studied the output of the triboelectric module at three different speeds of 8.4, 10.5, and 11.6 Hz in detail, which match typical freight train speeds of 80, 100, and 120 km $\mathrm{h}^{-1}$ as shown in Fig. 8(b). The time duration of the pulse signal matched nicely with the excitation speed. In addition, the HPT-RG may send the real-time speed of the vehicle to a receiver with the assistance of a Bluetooth transmission module.

We deployed the HPT-RG on the axle of the wheelset in a 1/2-scale freight wagon installed on rollers of a rig platform to investigate its actual output performance. The roller rig platform was equipped with two sets of transmission systems, consisting of triple-phase asynchronous motors, gearboxes, and rollers, as shown in Fig. 8(c). A control box continuously adjusted the motor speed, which drove the rollers via the gearbox. Hunan Railway High-speed Era Co., Ltd. machined the freight wagon, bogies, and rollers as standard C70, K6, and 75 kg $\mathrm{m}^{-1}$ in proportion, respectively. As a result, the rotational response of the wheelset axles was similar to that of the real vehicles. Moreover, compared to field trials, the roller rig is easy to control, convenient to operate, and cost-effective. Serving as an electronic load, the T/H2 is connected to the capacitor in the circuit of the prototyped HPT-RG. Figure 8(c) demonstrates the HPT-RG was capable of motivating T/H2 to transmit signals to the receiver at 11.6 Hz of the rig platform. To validate the feasibility, the bogie technology center of CRRC Tangshan Co., Ltd. carried out the reliability experiments of the prototype. The T/H2 effectively detected the axle temperature with the HPT-RG under the train speed of 120 km $\mathrm{h}^{-1}$ within 8 meters' transmission distance, which is the stable transmission distance of the T/H2 sensor. For long-distance transmission of information, we can utilize relay nodes for short transmission distances. In addition, there was no apparent mechanical damage in the HPT-RG after more than 600 h of official testing. In future work, the HPT-RG combines with a temperature sensor to form an all-in-one device mounted in the axle box to harvest the rotational energy of the wheelset due to the small volume and weight, which undoubtedly realizes integrated and self-powered axle temperature monitoring for vehicles. In addition, given that the impact force between the resonant and non-resonant beams increases under vertical vibration of the bogies, the HPT-RG improves output performance with the intensified transformation of the MFC and the effective contact area of the tribolayers.

## 5. Conclusions

In this work, we proposed the HPT-RG which not only harnesses mechanical energy for powering a temperature sensor but also serves as a speedometer to enable self-powered monitoring of freight rail transport. The rotational self-adaptive technique allows non-resonant beams to vibrate across a wide bandwidth under low-frequency excitations. In addition to promoting the output power of the MFC, the impact mechanism also established a self-sensing system with a triboelectric sensing module. We developed a theoretical model of HPT-RG to analyze the rotational self-adaptive and impact mechanisms. The optimization of the gap distance between the resonant and non-resonant beams resulted in high power generation at typical speeds for railways.

Theoretical and experimental results demonstrated that HPT-RG operated efficiently over an extensive bandwidth of 7-13 Hz, covering representative rotational frequencies of freight trains. The prototype possessed a maximum average power of 1.23 mW on optimal resistance of 200 kΩ at 13 Hz, with a corresponding power density of 55.52 μW $\mathrm{cm}^{-3}$ $\mathrm{Hz}^{-1}$, which was over 27 times that of traditional low-frequency rotary generators. The converted power allowed wireless sensors to transmit temperature data at a train speed of 120 km $\mathrm{h}^{-1}$. In addition, the triboelectric sensing module generated a pulse signal to detect the operation condition of the train wheel hub. This work demonstrates a novel concept for scavenging rotational energy from vehicles, presents a feasible scheme for freight train speed/mileage conditions, and offers promising prospects for self-powered wireless health monitoring networks in intelligent transportation applications.

## Appendix

### The developing dynamic models with different centrifugal force forms.

Figure A1 describes the dynamic models of the resonant beam with compressed and stretched effects. Referring to Fig. A1(a), the resonant beam moves towards the outside, resulting in compressed effects due to the centrifugal force of the inertial mass. This leads to reduced stiffness of the resonant beam, thereby approaching a softening beam without requiring additional apparatus. Conversely, in Fig. A1(b), the clamped end of the resonant beam is closer to the rotational center compared to its free end, resulting in the centrifugal force stretching the resonant beam and enhancing its stiffness to contribute to a hardening beam. The length of the resonant beam is $l_r$. Introducing the centrifugal force

$$F_c = m_t \Omega^2 (r + l_r), \tag{A1}$$

where $m_t$ is the tip mass of the resonant beam, and $r$ is the distance from the fixed end of the beam to the rotational center.

Centrifugal force is the axial tensile force of the resonant beam that can change the stiffness of the beam, thereby altering its corresponding resonant frequency [49]. The synthesized resonance frequency is

$$\omega_c = \omega \sqrt{1 + \frac{5}{14} \frac{F_c l_r^2}{EI}}, \tag{A2}$$

where the resonant beam's natural frequency $\omega = \sqrt{k_r / m}$. Then, the governing equation becomes

$$m\ddot{u} + c_r \dot{u} + (k_r + k_c - m\Omega^2) u = mg\cos(\Omega t), \tag{A3}$$

where $k_c = \frac{15}{14} \frac{r + l_r}{l_r} m_t \Omega^2$. The synthesized resonance frequency under the coupled gravity and centrifugal forces can be written as

$$\omega = \sqrt{\frac{k_r + k_c - m\Omega^2}{m}} = \sqrt{\omega^2 + \left[\frac{15 m_t (r + l_r)}{14 m l_r} - 1\right] \Omega^2}$$
$$= \sqrt{\omega^2 + M\Omega^2}. \tag{A4}$$

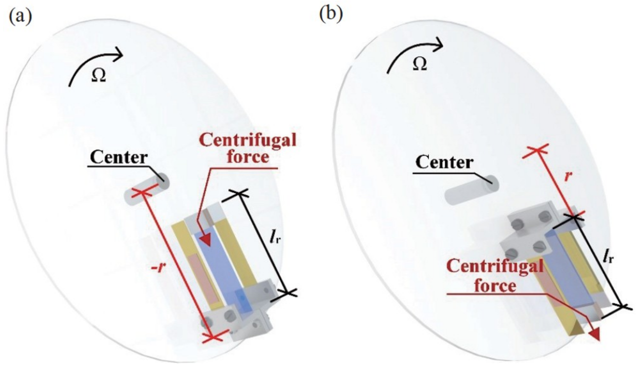

**Figure A1** Developing dynamic models (a) compressed and (b) stretched effect with different centrifugal forces for the resonant beam.

Based on Eq. (A4), the resonant frequency of the resonant beam varies with the external frequency, and $M$ denotes its adaptation index. For example, tuning the center distance $r$ and the resonant beam length $l_r$ varies the parameter $M$ to match the operation conditions. Note that $M = -1$ indicates the self-adaptive property of gravity during rotation. The hardening effect acts on the beam when the parameter $M$ is a positive number. Otherwise, the beam experiences a softening effect, as illustrated in Fig. A2. The softening beam ($M < 0$) has a narrower bandwidth and a higher amplitude than the one that ignores the self-adaptive mechanism ($M = 0$). In addition, as the parameter $M$ decreases, the resonant frequency approaches the low-frequency region, and the operation bandwidth reduces, but the amplitude increases. While the centrifugal force generates a stretched effect for the resonant beam, the positive frequency-adaptive effect enhances and eventually surpasses the negative frequency-adaptive effect of gravity as the external frequency grows, making $M$ larger than zero and exhibiting hardening characteristics.

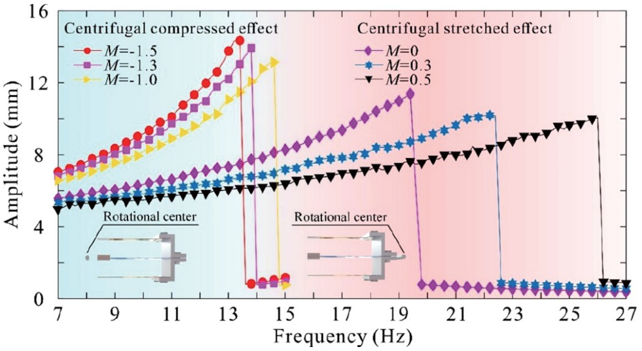

**Figure A2** Amplitude-frequency response of the resonant beam under different self-adaptive parameters *M*.

***Conflict of interest*** *On behalf of all authors, the corresponding author states that there is no conflict of interest.*

***Author contributions*** ***Zhixia Wang****: Conceptualization, Methodology, Data curation, Validation, Visualization, Funding acquisition, Writing – original draft.* ***Hongyun Qiu****: Visualization, Software.* ***Xuanbo Jiao****: Data curation, Validation.* ***Wei Wang****: Supervision, Funding acquisition, Writing – review & editing.* ***Qichang Zhang****: Supervision, Writing – review & editing.* ***Ruilan Tian****: Supervision, Writing – review & editing.* ***Dongxing Cao:*** *Formal analysis, Writing – review & editing.*

***Acknowledgements*** *The work was supported by the National Natural Science Foundation of China (Grant Nos. 12302022, 12172248, 12021002, and 12132010), Tianjin Research Program of Application Foundation and Advanced Technology (Grant No. 22JCQNJC00780), the State Key Laboratory of Mechanical Behavior and System Safety of Traffic Engineering Structures (Grant No. KF2024-09), and the IoT Standards and Application Key Laboratory of the Ministry of Industry and Information Technology (Grant No. 202306).*

1 J. Zuo, L. Dong, F. Yang, Z. Guo, T. Wang, and L. Zuo, Energy harvesting solutions for railway transportation: A comprehensive review, Renew. Energy **202**, 56 (2023).

2 G. Lederman, S. Chen, J. H. Garrett, J. Kovačević, H. Y. Noh, and J. Bielak, Track monitoring from the dynamic response of a passing train: A sparse approach, Mech. Syst. Signal Process. **90**, 141 (2017).

3 A. Hosseinkhani, D. Younesian, P. Eghbali, A. Moayedizadeh, and A. Fassih, Sound and vibration energy harvesting for railway applications: A review on linear and nonlinear techniques, Energy Rep. **7**, 852 (2021).

4 L. Dong, J. Zuo, T. Wang, W. Xue, P. Wang, J. Li, and F. Yang, Enhanced piezoelectric harvester for track vibration based on tunable broadband resonant methodology, Energy **254**, 124274 (2022).

5 Z. Wang, H. Du, W. Wang, Q. Zhang, F. Gu, A. D. Ball, C. Liu, X. Jiao, H. Qiu, and D. Shi, A high performance contra-rotating energy harvester and its wireless sensing application toward green and maintain free vehicle monitoring, Appl. Energy **356**, 122370 (2024).

6 S. Huo, P. Wang, H. Long, Z. Ren, Q. Yi, J. Dai, B. An, P. Wang, Y. Wang, M. Gao, and Y. Sun, Dual-mode electromagnetic energy harvester by Halbach arrays, Energy Convers. Manage. **286**, 117038 (2023).

7 L. C. Zhao, H. X. Zou, K. X. Wei, S. X. Zhou, G. Meng, and W. M. Zhang, Mechanical intelligent energy harvesting: From methodology to applications, Adv. Energy Mater. **13**, 2300557 (2023).

8 S. Sun, Y. Leng, S. Hur, F. Sun, X. Chen, H. C. Song, and C. Y. Kang, Force and stability mechanism analysis of two types of nonlinear mono-stable and multi-stable piezoelectric energy harvesters using cantilever structure and magnetic interaction, Smart Mater. Struct. **32**, 035003 (2023).

9 Y. Chen, Z. Yang, Z. Chen, K. Li, L. Wang, and S. Zhou, Theoretical and experimental investigations of multibifurcated piezoelectric energy harvesters with coupled bending and torsional vibrations, Acta Mech. Sin. **38**, 521434 (2022).

10 S. Gao, Q. Han, Z. Jiang, X. Zhang, P. Pennacchi, and F. Chu, Triboelectric based high-precision self-powering cage skidding sensor and application on main bearing of jet engine, Nano Energy **99**, 107387 (2022).

11 D. Tan, J. Zhou, K. Wang, C. Cai, and D. Xu, Modeling and analysis of the friction in a non-linear sliding-mode triboelectric energy harvester, Acta Mech. Sin. **38**, 521330 (2022).

12 W. Jiang, X. Han, L. Chen, and Q. Bi, Improving energy harvesting by internal resonance in a spring-pendulum system, Acta Mech. Sin. **36**, 618 (2020).

13 Y. Zhang, W. Wang, J. Xie, Y. Lei, J. Cao, Y. Xu, S. Bader, C. Bowen, and B. Oelmann, Enhanced variable reluctance energy harvesting for self-powered monitoring, Appl. Energy **321**, 119402 (2022).

14 F. Qian, S. Zhou, and L. Zuo, Improving the off-resonance energy harvesting performance using dynamic magnetic preloading, Acta Mech. Sin. **36**, 624 (2020).

15 Z. Wang, W. Wang, F. Gu, C. Wang, Q. Zhang, G. Feng, and A. D. Ball, On-rotor electromagnetic energy harvester for powering a wireless condition monitoring system on bogie frames, Energy Convers. Manage. **243**, 114413 (2021).

16 China Railway Transport Department, Introduction to Railway (China Railway Publishing House, Beijing, 2022).

17 D. Zhang, W. Zhai, and K. Wang, Dynamic interaction between heavy-haul train and track structure due to increasing axle load, Aust. J. Struct. Eng. **18**, 190 (2017).

18 L. Qi, L. Kong, Y. Wang, J. Song, A. Azam, Z. Zhang, and J. Yan, Recent progress in application-oriented self-powered microelectronics, Adv. Energy Mater. **13**, 2302699 (2023).

19 H. L. Fu, W. Z. Song, Y. Qin, and E. M. Yeatman, in Broadband vibration energy harvesting from underground trains for self-powered condition monitoring: Proceedings of the 2019 19th International Conference on Micro and Nanotechnology for Power Generation and Energy Conversion Applications (PowerMEMS), Krakow, 2019. pp. 1-5.

20 Z. Wang, W. Wang, L. Tang, R. Tian, C. Wang, Q. Zhang, C. Liu, F. Gu, and A. D. Ball, A piezoelectric energy harvester for freight train condition monitoring system with the hybrid nonlinear mechanism, Mech. Syst. Signal Process. **180**, 109403 (2022).

21 H. Fu, X. Mei, D. Yurchenko, S. Zhou, S. Theodossiades, K. Nakano, and E. M. Yeatman, Rotational energy harvesting for self-powered sensing, Joule **5**, 1074 (2021).

22 M. Guan, and W. H. Liao, Design and analysis of a piezoelectric energy harvester for rotational motion system, Energy Convers. Manage. **111**, 239 (2016).

23 L. Gu, and C. Livermore, Passive self-tuning energy harvester for extracting energy from rotational motion, Appl. Phys. Lett. **97**, 081904 (2010).

24 X. Rui, Z. Zeng, Y. Zhang, Y. Li, H. Feng, and Z. Yang, A design method for low-frequency rotational piezoelectric energy harvesting in micro applications, Microsyst. Technol. **26**, 981 (2020).

25 Z. Q. Lu, F. Y. Zhang, H. L. Fu, H. Ding, and L. Q. Chen, Rotational nonlinear double-beam energy harvesting, Smart Mater. Struct. **31**, 025020 (2022).

26 S. Orrego, K. Shoele, A. Ruas, K. Doran, B. Caggiano, R. Mittal, and S. H. Kang, Harvesting ambient wind energy with an inverted piezoelectric flag, Appl. Energy **194**, 212 (2017).

27 C. Wang, Y. Ji, S. K. Lai, Y. Liu, Y. Hao, G. Li, C. Wang, and G. L. Wen, A speed-amplified tri-stable piezoelectric-electromagnetic-triboelectric hybrid energy harvester for low-frequency applications, Nano Energy **114**, 108630 (2023).

28 S. Fang, N. Padar, M. J. Mirzaei, S. Zhou, and W. H. Liao, Disturbance rejection and performance enhancement of perturbed tri-stable energy harvesters by adaptive finite-time disturbance observer, Acta Mech. Sin. **38**, 521535 (2022).

29 P. Pillatsch, E. M. Yeatman, and A. S. Holmes, A piezoelectric frequency up-converting energy harvester with rotating proof mass for human body applications, Sens. Actuat. A-Phys. **206**, 178 (2014).

30 H. Fu, and E. M. Yeatman, Rotational energy harvesting using bi-stability and frequency up-conversion for low-power sensing applications: Theoretical modelling and experimental validation, Mech. Syst. Signal Process. **125**, 229 (2019).

31 H. X. Zou, W. M. Zhang, W. B. Li, Q. H. Gao, K. X. Wei, Z. K. Peng, and G. Meng, Design, modeling and experimental investigation of a magnetically coupled flextensional rotation energy harvester, Smart Mater. Struct. **26**, 115023 (2017).

32 B. Hu, J. Xue, D. Jiang, P. Tan, Y. Wang, M. Liu, H. Yu, Y. Zou, and Z. Li, Wearable exoskeleton system for energy harvesting and angle sensing based on a piezoelectric cantilever generator array, ACS Appl. Mater. Interfaces **14**, 36622 (2022).

33 H. Fu, S. Zhou, and E. M. Yeatman, Exploring coupled electromechanical nonlinearities for broadband energy harvesting from low-frequency rotational sources, Smart Mater. Struct. **28**, 075001 (2019).

34 L. Qi, H. Pan, Y. Pan, D. Luo, J. Yan, and Z. Zhang, A review of vibration energy harvesting in rail transportation field, iScience **25**, 103849 (2022).

35 L. Gu, and C. Livermore, Compact passively self-tuning energy harvesting for rotating applications, Smart Mater. Struct. **21**, 015002 (2012).

36 X. Rui, Y. Zhang, Z. Zeng, G. Yue, X. Huang, and J. Li, Design and analysis of a broadband three-beam impact piezoelectric energy harvester for low-frequency rotational motion, Mech. Syst. Signal Process. **149**, 107307 (2021).

37 S. Fang, S. Wang, G. Miao, S. Zhou, Z. Yang, X. Mei, and W. H. Liao, Comprehensive theoretical and experimental investigation of the rotational impact energy harvester with the centrifugal softening effect, Nonlinear Dyn. **101**, 123 (2020).

38 S. Fang, K. Chen, Z. Lai, S. Zhou, and W. H. Liao, Snap-through energy harvester with buckled mechanism and hierarchical auxetic

structures for ultra-low-frequency rotational excitations, Appl. Phys. Lett. **122**, 093901 (2023).

39 L. C. Zhao, H. X. Zou, Y. J. Zhao, Z. Y. Wu, F. R. Liu, K. X. Wei, and W. M. Zhang, Hybrid energy harvesting for self-powered rotor condition monitoring using maximal utilization strategy in structural space and operation process, Appl. Energy **314**, 118983 (2022).

40 J. M. Ramírez, C. D. Gatti, S. P. Machado, and M. Febbo, A piezoelectric energy harvester for rotating environment using a linked E-shape multi-beam, Extreme Mech. Lett. **27**, 8 (2019).

41 Y. Yang, Q. Shen, J. Jin, Y. Wang, W. Qian, and D. Yuan, Rotational piezoelectric wind energy harvesting using impact-induced resonance, Appl. Phys. Lett. **105**, 053901 (2014).

42 P. Tan, Q. Zheng, Y. Zou, B. Shi, D. Jiang, X. Qu, H. Ouyang, C. Zhao, Y. Cao, Y. Fan, Z. L. Wang, and Z. Li, A battery-like self-charge universal module for motional energy harvest, Adv. Energy Mater. **9**, 1901875 (2019).

43 Y. Pang, X. Zhu, C. Lee, and S. Liu, Triboelectric nanogenerator as next-generation self-powered sensor for cooperative vehicle-infrastructure system, Nano Energy **97**, 107219 (2022).

44 W. Wu, X. Cao, J. Zou, Y. Ma, X. Wu, C. Sun, M. Li, N. Wang, Z. Wang, and L. Zhang, Triboelectric nanogenerator boosts smart green tires, Adv. Funct. Mater. **29**, 1806331 (2019).

45 X. Zhao, G. Wei, X. Li, Y. Qin, D. Xu, W. Tang, H. Yin, X. Wei, and L. Jia, Self-powered triboelectric nano vibration accelerometer based wireless sensor system for railway state health monitoring, Nano Energy **34**, 549 (2017).

46 H. Yang, Y. Pang, T. Bu, W. Liu, J. Luo, D. Jiang, C. Zhang, and Z. L. Wang, Triboelectric micromotors actuated by ultralow frequency mechanical stimuli, Nat. Commun. **10**, 2309 (2019).

47 Q. Zheng, Y. Hou, H. Yang, P. Tan, H. Shi, Z. Xu, Z. Ye, N. Chen, X. Qu, X. Han, Y. Zou, X. Cui, H. Yao, Y. Chen, W. Yao, J. Zhang, Y. Chen, J. Liang, X. Gu, D. Wang, Y. Wei, J. Xue, B. Jing, Z. Zeng, L. Wang, Z. Li, and Z. L. Wang, Towards a sustainable monitoring: A self-powered smart transportation infrastructure skin, Nano Energy **98**, 107245 (2022).

48 H. Fu, and E. M. Yeatman, A methodology for low-speed broadband rotational energy harvesting using piezoelectric transduction and frequency up-conversion, Energy **125**, 152 (2017).

49 S. W. Shaw, and P. J. Holmes, A periodically forced piecewise linear oscillator, J. Sound Vib. **90**, 129 (1983).

# 具备能量采集和速度感知的复合式能量采集器及其自传感应用

王志霞, 邱宏蕴, 焦宣博, 王炜, 张琪昌, 田瑞兰, 曹东兴

**摘要** 实时车载健康监测系统对铁路行业保持高质量服务和运行安全至关重要. 然而, 目前监测系统中传感器的电源供应问题仍然存在, 特别是对于缺乏车载电源的货运列车. 为此, 本论文提出了一种用于车辆能量收集和速度感知的压电-摩擦电复合式旋转能量采集器(HPT-RG). HPT-RG借助旋转自适应技术软化驱动梁的等效刚度, 促使压电梁突破谐振的限制而工作在超低频领域. 实验表明, HPT-RG可以将列车的旋转能量转化为电能, 进而驱动无线温度传感器工作. 为了在列车轴箱有限空间内实现多维监测, HPT-RG增加了摩擦电传感模块来感知车辆的运行速度和里程. 此外, 样机在列车转向架轴箱轴承上进行了超过600 h的官方测试, 测试结果表明样机具有较好的机械耐久性. 本文提出的HPT-RG对于建立货运列车自供电、免维护和零碳车载无线监控系统至关重要.